CHAPTER VII
CATALYTIC ACTIVITY OF Au–Cu/CeO_2–ZrO_2 IN STEAM REFORMING OF METHANOL*

7.1 Abstract

Bimetallic Au–Cu/$Ce_{0.75}Zr_{0.25}O_2$ catalysts prepared by deposition-precipitation, were tested for steam reforming of methanol (SRM) in the range of 200–500 °C. Many effective parameters—Au/Cu atomic ratio, gas pretreatment, total metal loading, and calcination temperature—were investigated and correlated with catalyst properties. At the Au/Cu ratio of 1/3, the homogeneous Au–Cu alloy was found to be active for SRM, while an inhomogeneous or partially developed alloy formation was found after applying H_2 and O_2 pretreatments. There were no significant differences in catalytic activity with different total loadings and calcination temperatures; however, the 7 wt% Au–Cu catalyst calcined at 300 °C exhibited complete methanol conversion, 82 % H_2 selectivity, and 1 % CO selectivity at a low temperature of 300 °C. In regards to stability, the bimetallic catalyst displayed a long life, even though coke and metallic copper were formed.

Keywords: Steam Reforming of Methanol; Hydrogen; Alloy; Bimetallic; Au Catalyst

7.2 Introduction

Steam reforming of methanol (SRM) is one of the alternative ways to produce hydrogen (H_2). Due to its high purity product stream, this technique has received much attention as a potential technology to feed hydrogen to the proton exchange membrane fuel cells (PEMFCs) to generate an electricity [1]. Normally, SRM is more favorable at high temperatures because it is an endothermic reaction thus there is a requirement for heating the reagents. However, the main drawback of the SRM is the co-existence of a side reaction—methanol decomposition

---

*Applied Catalysis A: General, 456 (2013) 135–143.

(DM)—which is favored at high temperatures and also forms CO which poisons the Pt electrode in PEMFCs [2–4]. Low temperature (200–400 °C) SRM can be beneficial because of the lower amount of CO formed and energy saved. However, improvement of SRM activity at low-temperatures depends on many parameters, such as H_2O/CH_3OH molar ratio [5,6], the types of catalyst selection [7], reaction temperature [1,2], and gas hourly space velocity [4].

In this study, we focused on developing more active catalysts starting with the support. Ceria (CeO_2) support is attractive for SRM reaction since it has high oxygen vacancies to store the oxygen atoms of the feed reactants, and then release them in an active form to activate the reaction. This characteristic property of the CeO_2 has been widely used in water-gas shift reaction (WGSR) [8] and preferential CO oxidation (PROX) [9]. In addition, oxygen vacancies and redox properties of ceria have been improved by inserting cationic species ($M^{\delta+}$ where M = Fe, Zr, Mn, etc.) into the ceria lattice to form $Ce_xM_{1-x}O_2$ solid solutions, which have also significantly enhanced the catalytic activities in many reactions [2,10,11]. Among the mixed oxides supports, the CeO_2–ZrO_2 support has better thermal stability, smaller crystallite size, and lower coke formation—a major cause of catalyst deactivation [12,13]. Based on this we decided to use CeO_2–ZrO_2 as the support for our SRM catalyst. However, the creation in the efficient oxygen vacancies of the CeO_2–ZrO_2 support depends on the preparation route used [14,15].

For the active metal in the catalyst, we chose gold (Au) because of its well known CO oxidation activity [11,16]. Recent studies carried out in our laboratory with ceria and CeO_2–Fe_2O_3 found that the Au supported over CeO_2 and CeO_2–Fe_2O_3 exhibited the superior activity (100 % CH_3OH conversion) in the low-temperature range of 300–400 °C, with modest CO production (10 % v/v) [2,3,5]. The activity of gold catalysts strongly depends on the Au dispersion, Au particle size, the interaction between Au and the support, and the promotion by another active metal [2,17,18]. The combination of Cu and Au as a bimetallic catalyst has shown high catalytic activity in many reactions. The Au–Cu alloy was found to be an active phase [19–21], when compared to the individual Au and Cu catalysts. Likewise, the classification of Au–Cu alloy could be differentiated depending on (i) the origin of

the CuO species: highly dispersed and bulky types [22,23] and/or (ii) the oxidation states of the Cu species (Cu^{2+}, Cu^{+}, and Cu^{0}) [22]. Liu et al. also reported on the roles of Cu which helped prevent Au sintering and stabilize the Au particle size, as well as the Au dispersion [24].

In this study, a series of Au–Cu/CeO_2–ZrO_2 catalysts prepared by the deposition-precipitation technique (DP) were investigated for SRM in the 200 to 500 °C range. The parameters considered involved Au/Cu atomic ratio, gas pretreatment, total metal loading, and calcination temperature. The physical-chemical properties of the catalysts were characterized by means of XRF, XRD, H_2-TPR, UV-vis, TPO, and TEM.

7.3 Experimental

7.3.1 Catalyst preparation

The CeO_2–ZrO_2 mixed oxide support with Ce/(Ce+Zr) of 0.75 was initially prepared by the co-precipitation (CP) method to achieve a $Ce_{0.75}Zr_{0.25}O_2$ solid solution. Three 0.1 M aqueous solutions of cerium (III) nitrate hexahydrate ($Ce(NO_3)_3.6H_2O$; Aldrich), zirconium (IV) oxide chloride octahydrate ($ZrOCl_2.8H_2O$; Merck), and Na_2CO_3 (Riedel-de Haen) were mixed in appropriate amounts under vigorous stirring at 80 °C and pH of 8. Afterward, the precipitate was washed, dried, and calcined in air at 400 °C for 4 h in order to obtain the support.

For the second step, gold was deposited on the $Ce_{0.75}Zr_{0.25}O_2$ support with 3 wt% loading. An aqueous solution of $HAuCl_4.3H_2O$ (0.005 M, Alfa AESAR) was heated to 80 °C and adjusted to pH 8 with Na_2CO_3. After the resulting solution was stirred for 1 h, the suspension was washed with warm deionized water to eliminate the residue ions. The deionized precipitate was dried at 110 °C and calcined in air at 400 °C for 4 h. For the Cu/$Ce_{0.75}Zr_{0.25}O_2$ catalyst, the preparation was similar to gold deposition, but the metal solution was used as copper (II) nitrate trihydrate ($Cu(NO_3)_2.3H_2O$; MERCK), and the solution was adjusted to pH 7.

For the bimetallic Au–Cu/$Ce_{0.75}Zr_{0.25}O_2$ catalyst preparation, two metal aqueous solutions—$Cu(NO_3)_2.3H_2O$ and $HAuCl_4.3H_2O$—were used as

depositing agents, and then heated to 80 °C with the pH adjusted to 7 by an addition of Na_2CO_3. The appropriate amounts of mixing solutions followed the Au/Cu ratio of 3/1, 1/1, and 1/3. The total loading was varied in the range of 3–7 wt% under the suitable Au/Cu ratio. After the resulting solution was stirred for 1 h, the suspension was washed and dried as same as the deposition step. Finally, the catalyst was calcined in air at various temperatures (200-400 °C) for 4 h.

7.3.2 Catalyst characterization

An X-Ray Fluorescence Spectrometry, XRF (AXIOS PW4400) was used to determine the actual surface (Au, Cu, Ce, and Zr) composition.

The XRD measurement was carried out on a JEOL X-Ray diffractometer system (JDX-3530) with a CuK_α (1.5406 Å) X-ray source operating at 40 kV and 30 mA.

The size and distribution of the Au particles deposited on the supports were directly observed by a transmission electron microscope, TEM (JEOL, JEM 2010), at an accelerating voltage of 200 kV in bright field mode. Before being transferred into the TEM chamber, the samples were dispersed in ethanol and then dropped onto a copper grid. The volume-area average Au particle size diameter (d_{TEM}) was calculated from the following formula: $d_{TEM} = \Sigma(n_i d_i^3)/(n_i d_i^2)$, where n_i is the number of Au particles of diameter d_i.

The UV-vis spectroscopy experiments checked for the presence of different states of oxidation of the contained metals (which were recorded on a Shimadzu UV spectrophotometer 2550). The measurements were performed on air-exposed samples at ambient temperature between 200 and 800 nm. The absorption intensity was expressed using the Kubelka-Munk function, $F(R\infty) = (1-R\infty)^2/(2R\infty)$, where $R\infty$ is the diffuse reflectance from a semi-infinite layer.

Temperature-programmed reduction (TPR) was utilized for the evaluation of the reducibility of the catalysts and was used with 10 % H_2 in Ar at 30 mL/min as the reducing gas in a conventional TPR reactor equipped with a thermal conductivity detector. The reduction temperature was raised from 30 to 850 °C at a ramp rate of 10 °C/min.

The amount of carbon formation on the spent catalysts was measured by means of temperature-programmed oxidation (TPO). About 50 mg of the powdered samples was packed in a quartz tube reactor before being heated from 100 °C, with a heating rate of 12 °C/min, to 900 °C under a flow of 2 % O_2/He, at using a gas flow rate of 30 mL/min.

7.3.3 Catalytic activity measurements

The SRM reaction was carried out in a fixed-bed reactor containing 100 mg of 80 to 120 mesh Au–Cu/CeO_2–ZrO_2 catalysts under atmospheric pressure with a reaction temperature of 200 to 500 °C. A mixture of distilled water and methanol in a syringe was injected continuously by a syringe pump at a rate of 1.5 mL h^{-1} to a vaporizer to produce a vapor of methanol and steam, which was mixed with the He carrier gas before entering the catalytic reactor. The H_2O/CH_3OH molar ratio was fixed at 2/1. For the gas pretreatment, the 3 wt% of the optimum Au/Cu ratio was chosen for further pretreating with H_2 and O_2 gases at 200 °C for 2 h before testing the SRM. The total metal loadings and calcination temperatures were varied from 3 to 7 wt% and 200 to 400 °C, respectively. The stability tests of the Cu/$Ce_{1-x}Zr_xO_2$, Au/CeO_2–Fe_2O_3 [2], and Au–Cu/$Ce_{1-x}Zr_xO_2$ were investigated on stream for 18 hours for comparison purposes. The gas hourly space velocity (GHSV) was 21 000 mL/g-cat. h. The product gases (e.g. H_2, CO, CO_2, and CH_4) from the reactor were analyzed both qualitatively and quantitatively by auto-sampling in an on-line gas chromatograph, Agilent 6890N, with a packed carbosphere (80/100 mesh) column (10 ft x 1/8 inch) and a thermal conductivity detector (TCD). The selectivity of each product gas was defined by the mole percentage in the product stream. No methane formation was observed.

7.4 Results and discussion

7.4.1 Catalyst characterization

According to the chemical composition of each catalyst, as recorded in Table 7.1, most catalysts have actual metal compositions close to those of the

expected values, including the Ce and Zr compositions. However, the Au3Cu1 sample has the actual Au/Cu ratio of 1.61, which is less than the expected value of 3, indicating a deviation of Au and Cu concentrations during the preparation step. The chemical and physical properties of the bimetallic Au–Cu/$Ce_{0.75}Zr_{0.25}O_2$ catalysts are summarized in Table 7.2. The lattice constant (a_0) of the ceria in the CeO_2–ZrO_2 mixed oxides was 0.539–0.540 nm, which was smaller than that of pure CeO_2 (0.544). This is attributed to the formation of a stable $Ce_{1-x}Zr_xO_2$ solid solution [14,23], resulting in the shrinkage of the lattice parameter [25,26]. For the XRD patterns of the catalysts with various Au/Cu ratios, as presented in Fig. 7.1A, no copper species diffractions are observed, implying that if pure copper or copper oxide were formed, their crystallite sizes were very small [23,24]. In comparison to pure Au/$Ce_{0.75}Zr_{0.25}O_2$ (Au/Cu = 1/0), the Au (111) diffraction peaks started to shift from 38.34° to 38.17° in the presence of Cu loading, as presented in Fig. 7.2A. Moreover, this diffraction in the bimetallic catalyst became broader after loading higher Cu concentrations. All of these changes were related to the formation of Au Cu alloy particles [23,24]. According to Bragg's equation, Au_xCu_{1-x} intermetallic alloys could be evidenced from the change in the lattice constant of the alloy diffraction, which was 0.4050–0.4076 nm, located between the pure gold (0.4079 nm) and copper (0.3615 nm) [17]. However, these values deviated from those calculated from Vegard's law, probably due to the disordering in the Au_xCu_{1-x} structure [17]. Using Scherrer's equation, the average CeO_2 crystallite size was found to be increased from 7 to 9 nm, and the significant growth in Au crystallite sizes were also observed on the bimetallic catalysts, postulating that the Au–Cu alloy particles could improve both Au crystal growth and the crystallite size of the support [23]. Among the bimetallic catalysts, the rich Au mixture (Au/Cu = 3/1) had the highest Au crystallite size, while the rich Cu mixture (Au/Cu = 1/3 and 1/1) crystallites were smaller. The possible explanation was that high amounts of Cu prevented Au sintering during the preparation step. This was in accordance with the previously proposed core-shell model of the Au–Cu catalysts in regards to preventing sintering of Au [24]. For the CeO_2 crystallite size, the largest crystallite size belonged to the Au/Cu of 1/1 sample, while the high Au concentration (Au/Cu = 3/1)

seemed to decrease the crystallite size. This revealed that the variation in CeO_2 crystallite size was dependent on the Au/Cu ratio as well.

As shown in Fig. 7.1B and Fig. 7.2B, it was found that the alloy diffraction of 38.17° shifted to 38.57° and 38.35°, which close to the characteristic Au (111) [3], after applying both H_2 and O_2 pretreatments, respectively. These observations revealed that the gas pretreatment could inhibit uniform alloy formation. The larger crystallite of the Au or Au–Cu alloy, as calculated from Au (111), was another outcome of H_2 pretreatment (from 14.81 nm to 20.61 nm), while the O_2 pretreated sample did not significantly change the Au or alloy crystallite size. When varying the total metal loading from 3 to 7 wt% (Fig. 7.1C), the sharpest Au diffraction was observed on the highest metal loading, indicating increasing crystallite size. The Au crystallite size was also a strong function of calcination temperature becoming undetectable by X-rays at a 200 °C calcination temperature (Fig. 7.1D),

Table 7.1 Chemical composition of bimetallic Au–Cu/$Ce_{0.75}Zr_{0.25}O_2$ catalysts

Catalyst	Total loading (wt%)	Calcination temperature (°C)	Au* (wt%)	Cu* (wt%)	Ce* (wt%)	Zr* (wt%)	Synthesized Au/Cu ratio	Expected Au/Cu ratio
Au1Cu0	3	400	2.92	-	81.18	15.90	-	-
Au1Cu3	3	400	1.47	1.37	82.63	14.53	0.35	0.33
Au1Cu3 (H_2 pretreatment)	3	400	1.44	1.54	81.63	15.40	0.30	0.33
Au1Cu3 (O_2 pretreatment)	3	400	1.45	1.57	81.41	15.57	0.30	0.33
Au1Cu1	3	400	1.90	0.77	81.52	15.81	0.80	1.00
Au3Cu1	3	400	2.13	0.43	81.46	15.99	1.61	3.00
Au1Cu3	5	400	2.44	2.51	79.66	15.39	0.31	0.33
Au1Cu3	7	400	3.47	3.54	79.08	13.91	0.32	0.33
Au1Cu3	7	300	3.27	3.53	79.06	14.15	0.30	0.33
Au1Cu3	7	200	3.61	3.41	79.06	13.92	0.34	0.33
Au0Cu1	3	400	-	5.18	83.24	11.58	0.00	0.00
Spent Au1Cu3	7	300	3.34	3.63	79.95	13.07	0.30	0.33

*measured by XRF.

Table 7.2 Chemical and physical properties of bimetallic Au–Cu/$Ce_{0.75}Zr_{0.25}O_2$ catalysts

Catalyst	Total loading	Calcination temperature	Crystallite size (nm)[a]		Lattice constant (nm)[b]	
	(wt%)	(°C)	CeO_2	Au	CeO_2	Au
Au1Cu0	3	400	7.21	7.78	0.539	0.4076 (0.4076)[c]
Au1Cu3	3	400	7.26	14.81	0.540	0.4050 (0.3753)
Au1Cu3 (H_2 pretreatment)	3	400	9.09	20.61	0.540	0.4038
Au1Cu3 (O_2 pretreatment)	3	400	6.65	13.53	0.539	0.4076
Au1Cu1	3	400	9.68	16.14	0.540	0.4063 (0.3877)
Au3Cu1	3	400	8.07	22.16	0.540	0.4076 (0.3985)
Au1Cu3	5	400	7.66	13.51	0.540	-
Au1Cu3	7	400	7.83	23.15	0.540	-
Au1Cu3	7	300	7.79	13.19	0.540	-
Au1Cu3	7	200	6.90	-	0.540	-
Au0Cu1	3	400	8.35	-	0.540	-
Spent Au1Cu3	7	300	8.73	-	0.543	0.3952

[a] Mean ceria crystallite sizes were calculated from the average values of CeO_2 (111), (220), and (311), while the Au crystallite sizes were calculated from the Au (111).

[b] Unit cell parameters calculated from CeO_2 (220) and Au (111) with the Bragg's equation.

[c] Unit cell parameters calculated from Vegard's law.

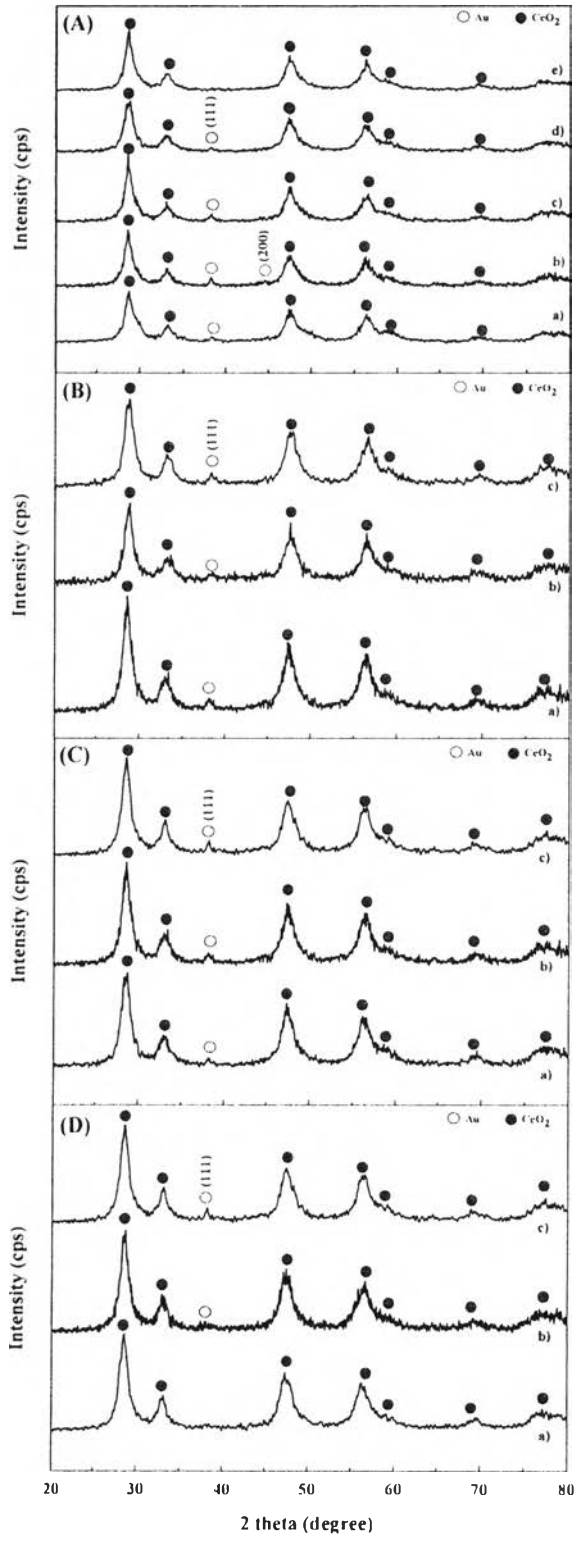

Figure 7.1 XRD patterns of the Au–Cu/$Ce_{0.75}Zr_{0.25}O_2$ catalysts: (A) Effect of Au/Cu atomic ratios with 3 wt% loading; (a) Au1Cu0, (b) Au3Cu1, (c) Au1Cu1, (d) Au1Cu3, and (e) Au0Cu1. (B) Effect of gas pretreatments on 3 wt% Au1Cu3; (a)

unpretreatment, (b) H_2 pretreatment, and (c) O_2 pretreatment. (C) Effect of total loading on Au1Cu3; (a) 3 wt%, (b) 5 wt%, and (c) 7 wt%. (D) Effect of calcination temperatures on 7 wt% Au1Cu3 calcined at; (a) 200 °C, (b) 300 °C, and (c) 400 °C.

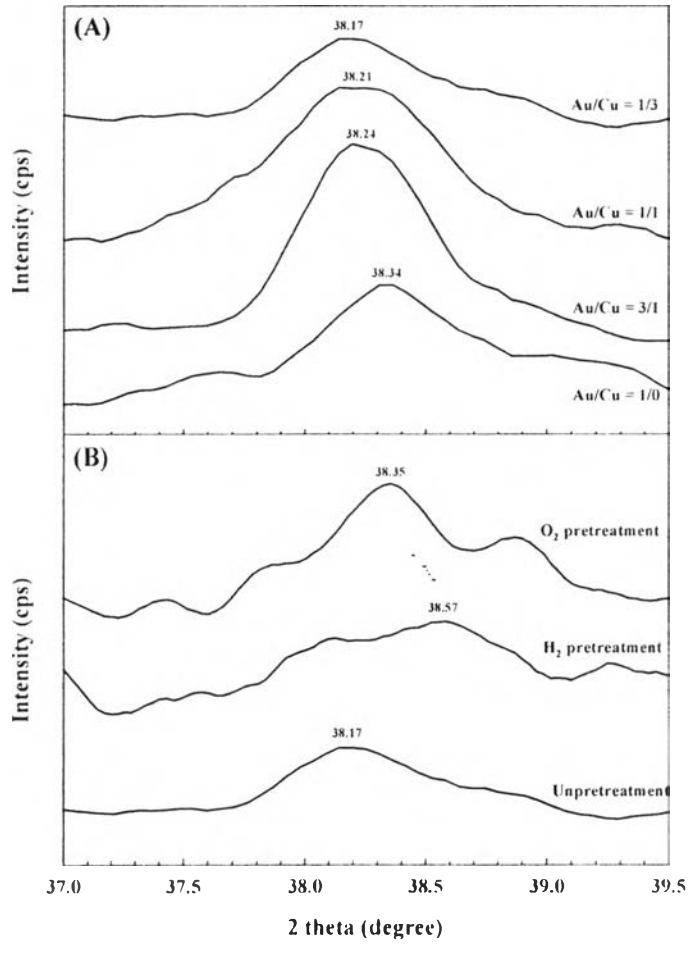

Figure 7.2 XRD patterns of the Au diffractions in the Au–Cu/$Ce_{0.75}Zr_{0.25}O_2$ catalysts: (A) Effect of Au/Cu atomic ratios with 3 wt% loading. (B) Effect of gas pretreatments on 3 wt% Au1Cu3.

In order to identify the Au species, Au^{3+}, Au cluster, and Au^0, UV-spectra was used (Fig. 7.3). The absorption band of Au^{3+} at 250 nm [27] was difficult to detect because this band overlapped the much stronger band of the mixed oxides support at 260–290 nm, which was located between the bands of pure CeO_2 and ZrO_2 at 343–345 nm and 208–210 nm (not shown here), respectively [23,28]. In addition, all of the mixed oxides spectra had no change in absorption position, indicating that

the solid solution phase was uniform and stable. The metallic (Au^0) band at 500–600 nm [2,3,29] increased with increasing Au/Cu ratio from 1/3 to 3/1. This could be due to the increase of Au concentration and/or Au crystallite size [3].

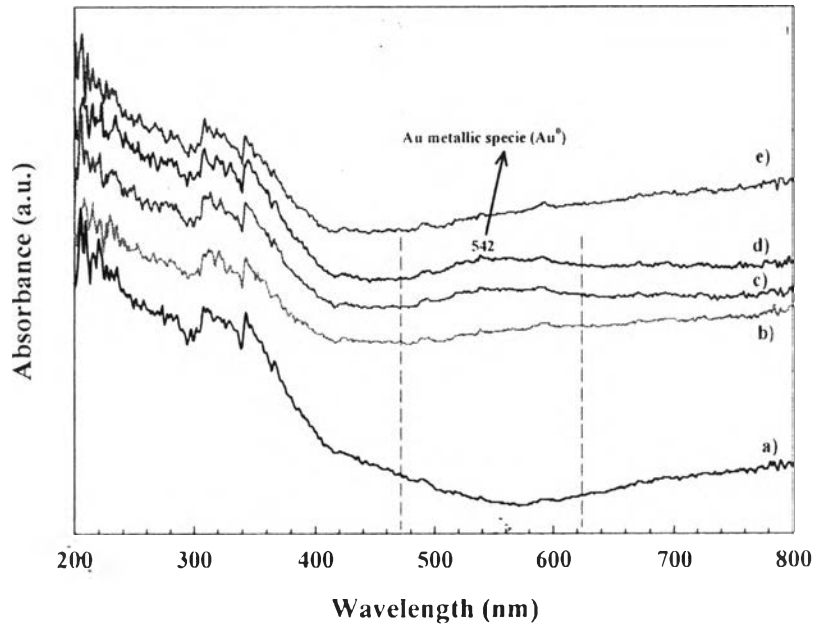

Figure 7.3 Diffuse reflectance UV–vis spectra of the Au species in various Au/Cu atomic ratios; (a) Au0Cu1, (b) Au1Cu3, (c) Au1Cu1, (d) Au3Cu1, and (e) Au1Cu0.

The TPR profiles of all bimetallic catalysts are shown in Fig. 7.4. In the case of 3 wt% Au–Cu/CeO_2–ZrO_2 with various Au/Cu atomic ratios (Fig. 7.4A), the Au/CeO_2–ZrO_2 presented four reduction peaks, two temperature peaks of 121 and 149 °C, which were assigned to the reductions of $Au^{3+} \rightarrow Au^0$ and $Au^+ \rightarrow Au^0$, respectively [30,31]. The two high temperature peaks were due to the reduction of the ceria surface at 519 °C and the bulk ceria at 825 °C (not shown here) [2,3,23]. For the Cu/CeO_2–ZrO_2, the lowest temperature peak at 155 °C was assigned to the reduction of highly dispersed or small CuO particles strongly interacting with the support, while the higher temperature at 183 °C corresponded to the reduction of the bulk or larger CuO particles that had weak interaction with the support [22,23]. For Au to Cu ratio of 3/1, there were three main peaks at 125, 162, and 192 °C. The shifts in the observed temperatures were due to the overlap of the pure gold and copper peaks, and it is actually possible that alloy formation between Cu and Au is

responsible for some of the shifts. However, it is not possible to clarify the chemical structure of the alloy, based on the TPR spectra. When decreasing the Au/Cu ratio from 3/1 to 1/1, all three peaks shifted to lower temperatures, possibly due to the formation of an easily reducible small crystallite size alloy between Au and Cu. The Cu rich catalyst (Au/Cu of 1/3), is dramatically different; almost all of the pure gold and copper peaks have disappeared. In the low temperature region, only two peaks were observable. Firstly, the Au reduction began shifting to the lowest temperature at 103 °C with the lowest intensity. The second was that some part of the Au peak overlapped with the highly dispersed CuO reduction, and then merged together as the symmetric bell shape at the same temperature (159 °C), while the bulk CuO disappeared. The same kind of symmetric reduction peak has been reported in the Pd-Cu bimetallic catalyst that the Pd and Cu could form a homogeneous $PdCu_x$ alloy [32]. Consequently, the Au–Cu symmetric peak was also referred to the interaction between $Au^{\delta+}$ and highly dispersed CuO to form alloy, while the bulk CuO had less interaction in this case [21].

Taking into account the size effect, the change in Au reduction resulted in a change in Au particle size. The lower Au reduction temperature, with increasing Cu content, corresponded to the smaller Au crystallite sizes, which were reduced much easier than the larger ones. Besides, the higher intensity of the alloy peak could be defined as the smaller crystallite size, which provides more surface area for H_2 to spill over the surface as well [33]. It was reasonable to conclude that CuO displayed both a core-shell model around the Au particles, and a partially-formed alloy with the Au particles.

After applying the gas pretreatment (Fig. 7.4B), the lack of a homogeneous alloy phase was evidenced by the existence of CuO reduction. For the O_2 pretreated sample, both CuO reductions shifted toward higher temperatures, implying that small and bulk CuO particles were generated. Furthermore, the sharp peak and high intensity of the bulk CuO represented the large CuO particles isolated on the surface. For the H_2 pretreated sample, lower intensities of both CuO types were observed, which was related to the lower amounts of the CuO species. In addition, the shift of the Au reduction to 127 °C corresponded to the growth of Au

particle or crystallite, which was in line with the XRD results. When varying the total metal loading in the Au/Cu of 1/3 sample (Fig. 7.4C), the shapes of alloy reductions were still almost symmetric at 5 and 7 wt%, which attributed to the similar Au–Cu interaction in the Au_1Cu_3 alloy phase. The remarkable increase in alloy intensities represented to the strong alloy–support interaction, where better reducibility of the contact area between the alloy particles and the support occurred after increasing the amounts of active species (alloy) and/or total metal loading [17,34]. The shift in the alloy peak towards higher temperatures (159→188 °C) represented the increase in alloy particle size [17], with the 7 wt% sample being the largest.

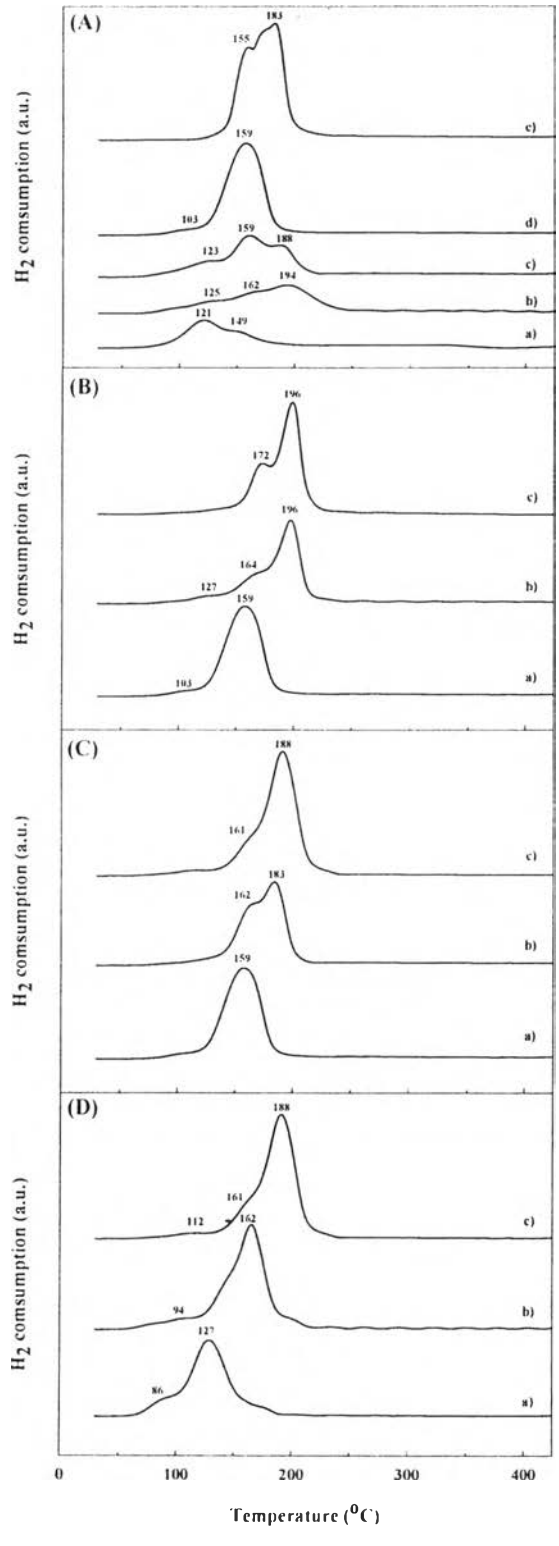

Figure 7.4 TPR profiles of the Au–Cu/$Ce_{0.75}Zr_{0.25}O_2$ catalysts: (A) Effect of Au/Cu atomic ratios with 3 wt% loading; (a) Au1Cu0, (b) Au3Cu1, (c) Au1Cu1, (d) Au1Cu3, and (e) Au0Cu1. (B) Effect of gas pretreatments on 3 wt% Au1Cu3; (a)

unpretreatment, (b) H_2 pretreatment, and (c) O_2 pretreatment. (C) Effect of total loading on Au1Cu3; (a) 3 wt%, (b) 5 wt%, and (c) 7 wt%. (D) Effect of calcination temperatures on 7 wt% Au1Cu3 calcined at; (a) 200 °C, (b) 300 °C, and (c) 400 °C.

When lowering the calcination temperature below 400 °C in the 7 wt% catalyst (Fig. 7.4D), the alloy reduction shifted towards the lower temperature (188→127 °C), which implies that the alloy size became smaller at the low calcination temperature. Likewise, the alloy–support interaction was not improved due to lower hydrogen consumption (intensity). Interestingly, higher intensities at the lowest reduction temperature (86 and 94 °C) were pronounced at a lower calcination temperature, which was ascribed to the presence of more reactive sites and Au species at the interface between the alloy particle and the support [17]. The possible explanation is that the high calcination temperature caused a decrease in the number of the reactive atoms located at the interface between the alloy particle and the support since the Cu enrichment entirely covered the reactive sites (or Au) on the surface instead, as confirmed by the likely-disappearance of the lowest TPR peak [17]. To better understand the above explanation, a schematic drawing is shown in Fig. 7.5B.

In order to evaluate the true size of the alloy particles, TEM images were taken (Fig. 7.6). Because of the difficulty in detecting the individual Au or Cu particles in the uniform alloy phase, the average Au–Cu particle size was used for evaluation [19,21,23]. The alloy size of the 3 wt% Au1Cu3 catalyst was measured at 31.48 nm, which was close to that of 3 wt% Au/CeO_2–ZrO_2 (30.16 nm). We elucidated that the suitable alloy size for the SRM activity was approximately 32 nm.

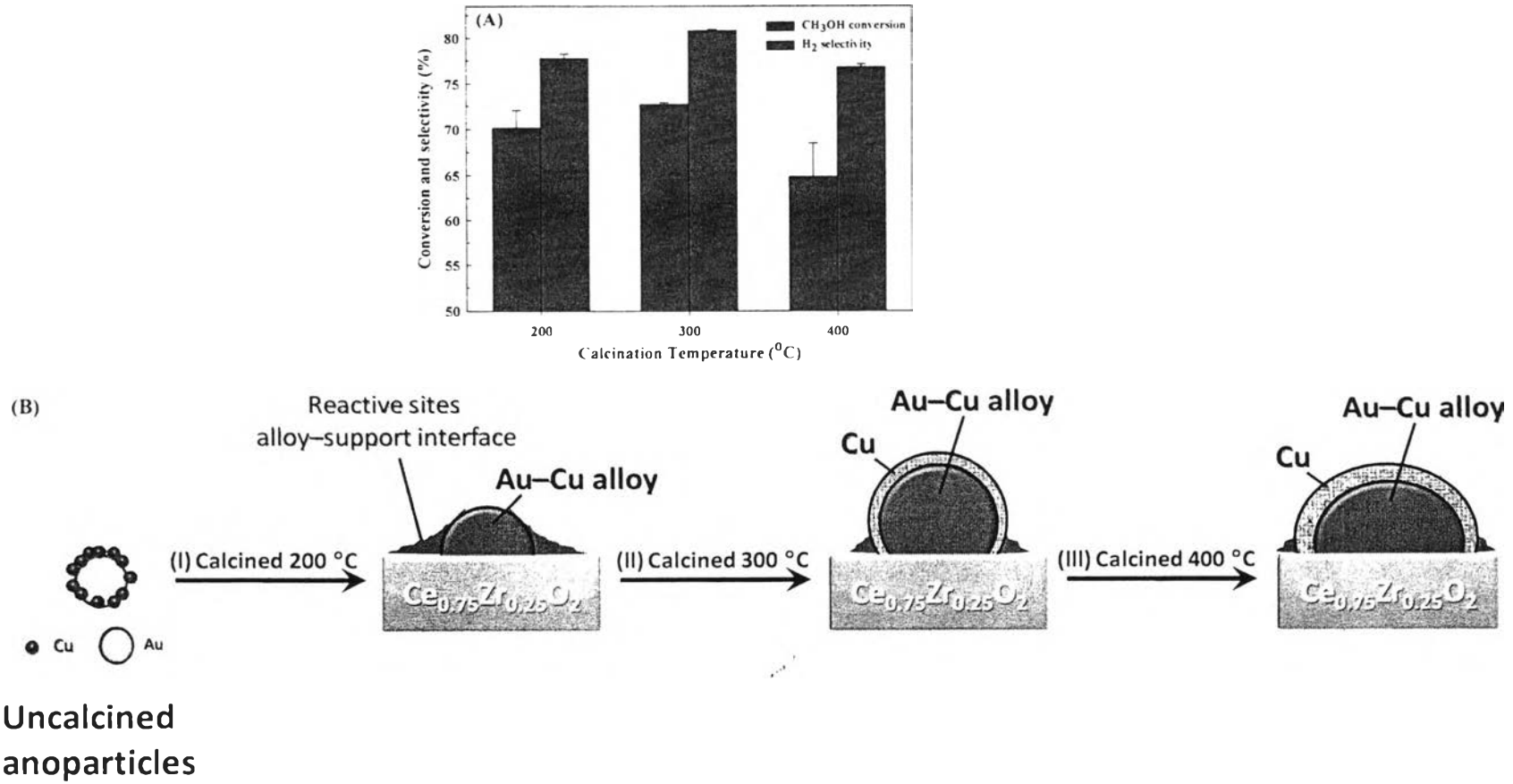

Figure 7.5 Effect of calcination temperature on methanol conversion over (A) 7 wt% Au–Cu/$Ce_{0.75}Zr_{0.25}O_2$, and (B) schematic drawing of the 7 wt% Au1Cu3/$Ce_{0.75}Zr_{0.25}O_2$ catalyst after calcination at various temperatures: (I) small alloy particles were formed with the presence of high reactive sites at the alloy–support interface; at higher calcinations temperatures (II) and (III), the alloy size increased, and the Cu enrichment covered either the reactive sites or the catalyst surface.

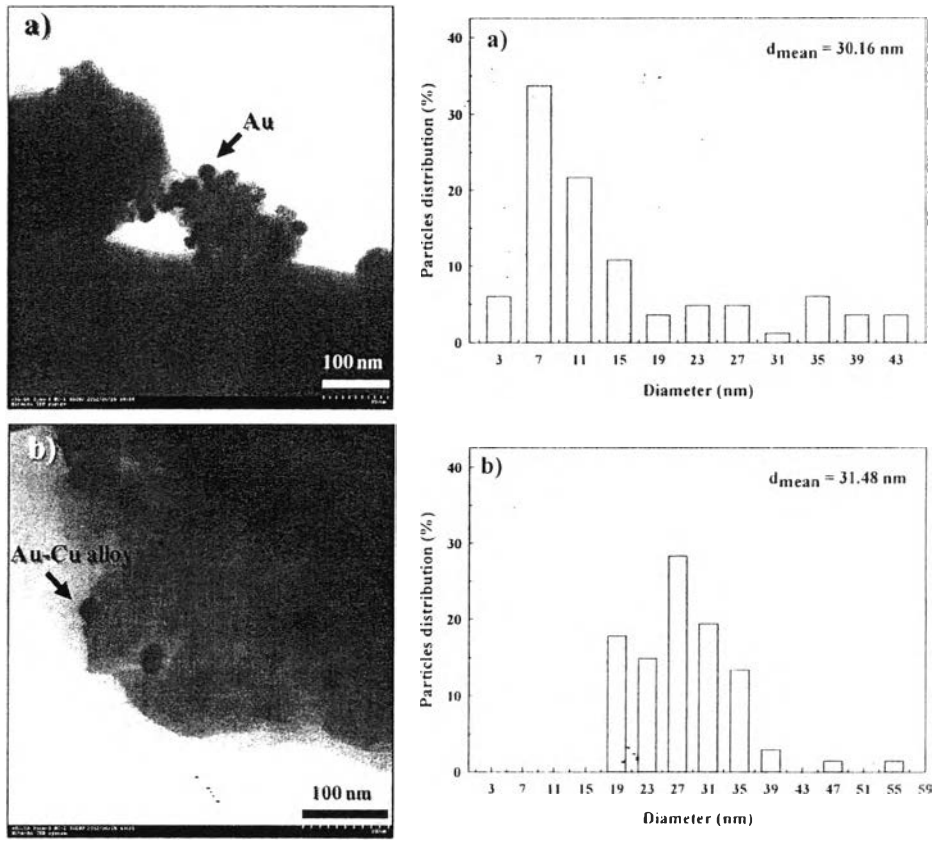

Figure 7.6 TEM images of Au and Au–Cu particle size distributions: (a) 3 wt% Au1Cu0; (b) 3 wt% Au1Cu3.

7.4.2 Catalytic activity

7.4.2.1 Effect of Au/Cu atomic ratio

The variation of Au/Cu composition significantly affected the catalytic activity of SRM (Fig. 7.7). The overall trends of the methanol conversion, hydrogen yield (not shown here), and gas selectivity were found to increase with reaction temperature according to the endothermic reaction. It is clear that Cu/CeO_2–ZrO_2 is a better catalyst in terms of more selectivity towards H_2. Gold is active too, but not as much as Cu. Among the bimetallic catalysts, the results revealed that the higher the Cu concentration, the more improved the catalytic activity became, whereas the Au3Cu1 did not follow the same trend due to its lowest catalytic activity. The full methanol conversion at $T \geq 350$ °C was observed in both Au1Cu3 and the pure Cu catalysts. However, the highest activity still belonged to the pure Cu

sample. In regards to CO selectivity, there was no significant difference between the catalysts below 400 °C, and only a small difference in H_2 selectivity was observed.

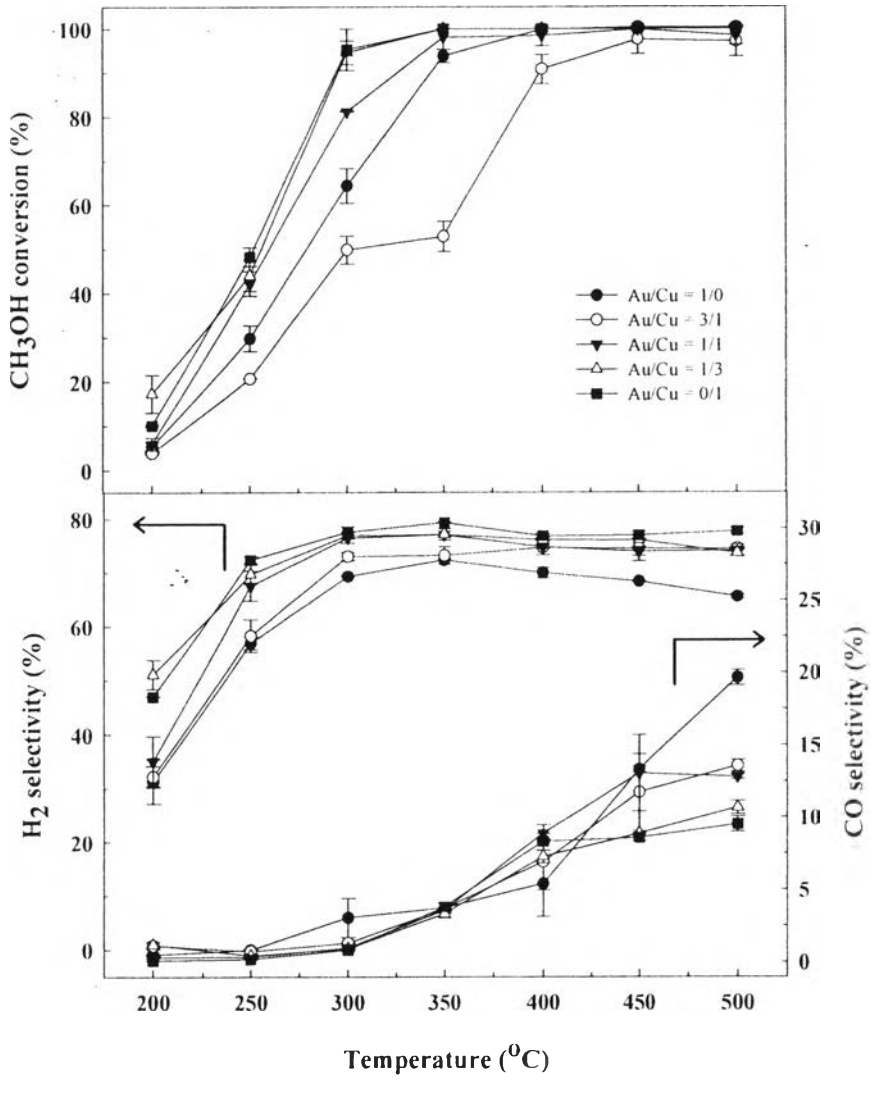

Figure 7.7 Effect of Au/Cu atomic ratios on methanol conversion and product selectivity over 3 wt% Au–Cu/$Ce_{0.75}Zr_{0.25}O_2$. (Reaction conditions: H_2O/CH_3OH, 2/1; calcination temperature, 400 °C.)

7.4.2.2 Effects of gas pretreatment, total loading, and calcination temperature

There is much literature interpreting the effect of gas pretreatment on fresh catalysts because this treatment can improve the chemical-physical change on the catalyst surface in terms of the active phase and its interaction

[35]. The results surprisingly indicated that all pretreated samples showed no improvement in catalytic activity through the entire range of reaction temperatures, when compared to the unpretreated sample, while the gases selectivities were almost the same in all samples. Similarly, there was no significant activity or selectivity difference between the different loadings at high temperatures. Nonetheless, the 7 wt% catalyst slightly facilitated the catalytic activity in 200–300 °C range. Again, there was no dependence on the calcination temperature in the 7 wt% Au–Cu/CeO_2–ZrO_2 under a Au/Cu atomic ratio = 1/3 and reaction temperature of 250 °C. However, the thermal treatment at 300 °C was chosen for the catalyst preparation due to its slightly higher catalytic activity, as evidenced in Fig. 7.5A.

7.4.3 Stability testing

In order to achieve the best performance of the catalyst, the low-temperature stability test was tested at 300 °C, as illustrated in Fig. 7.8. The Au/CeO_2–Fe_2O_3 catalyst was also tested for comparison purposes. The rapid deactivation of the Au/CeO_2–Fe_2O_3 (after 3 h), according to an unstable $Ce_xFe_{1-x}O_2$ solid solution during the reaction, had been clarified in our previous work [2]. Apparently, both the Cu/CeO_2–ZrO_2 and Au–Cu/CeO_2–ZrO_2 catalysts exhibited much better stability and catalytic activity, attributing to better thermal stability of the $Ce_xZr_{1-x}O_2$ solid solution phase. The Cu catalyst was stable to 10 h, while the Au–Cu catalyst had superior stability with a full methanol conversion in the entire time-on-stream, suggesting that the advantage of the Au–Cu alloy was the ability to delay this phenomenon. For the product selectivities, the average selectivities of H_2 and CO were observed as follows: 70 % and 3–5 % for the Au/CeO_2–Fe_2O_3, 78 % and 1–2 % for the Cu/CeO_2–ZrO_2, and 80 % and 0–1 % for the Au–Cu/CeO_2–ZrO_2, respectively. It was clearly seen that the formation of the Au–Cu alloy dramatically increased the SRM activity by increasing the H_2 production, when compared to the monometallic catalysts. Likewise, the CO concentration was low enough (< 1 % or 10 000 ppm) for further application in the PROX unit in the methanol fuel processor (MFP) (which will be carried out in the future work).

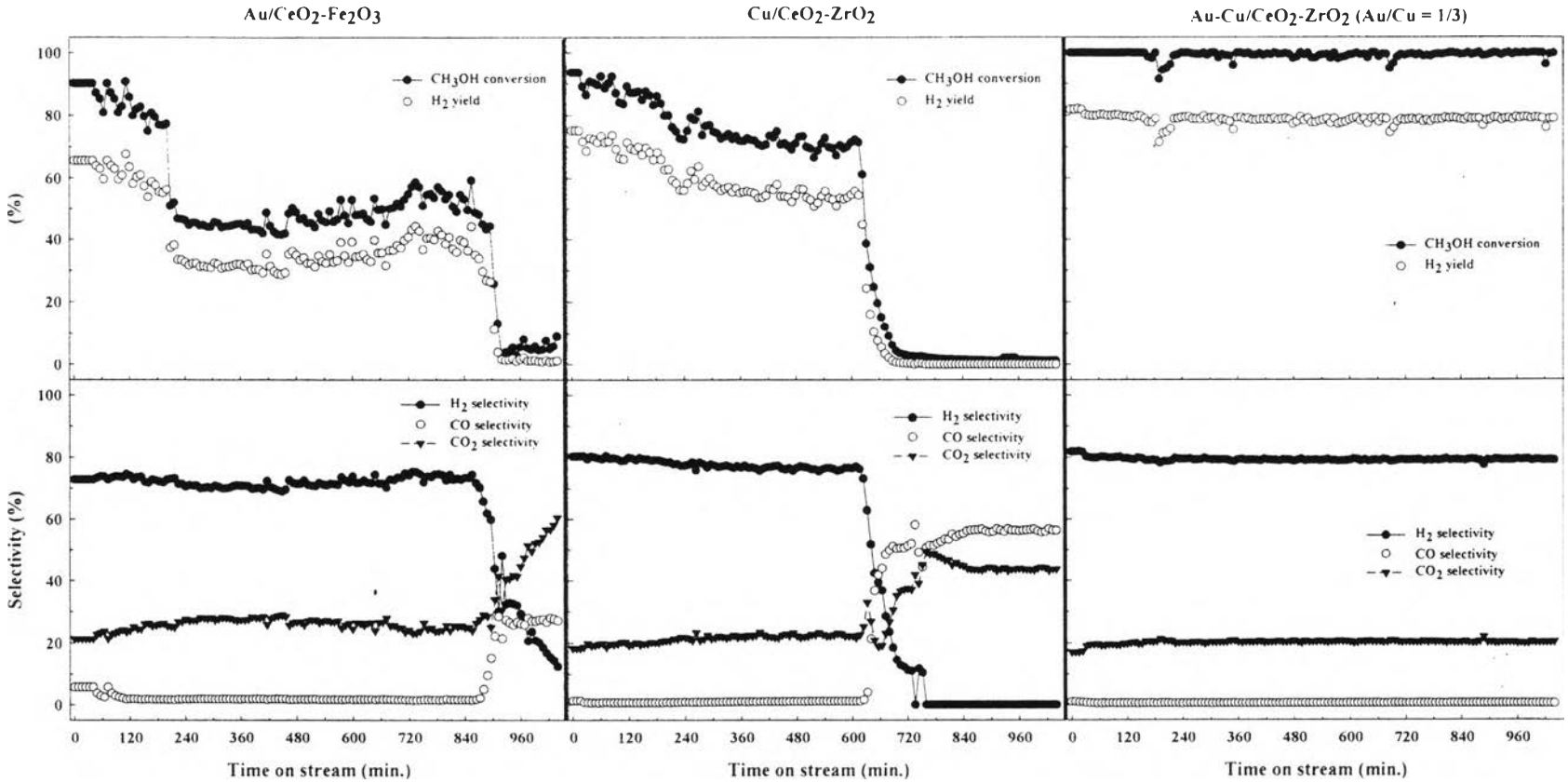

Figure 7.8 Comparison of stability testing of $Au/CeO_2–Fe_2O_3$, $Cu/CeO_2–ZrO_2$, and $Au–Cu/CeO_2–ZrO_2$ catalysts (Au/Cu atomic ratio = 1/3 and Ce/Zr = 3/1). (Reaction conditions: H_2O/CH_3OH, 2/1; reaction temperature, 300 °C; and time-on-stream per sample, 18 h)

In order to check the phase transformation of the spent catalyst after exposure to the reaction, XRD was used (Fig. 7.9). None of the free ZrO_2 particles or agglomeration of ZrO_2 particles was observed in the spent Au–Cu/CeO_2–ZrO_2 catalyst, while the intensities of CeO_2 diffractions at 28.5° (111) and 47.47° (220) slightly decreased after exposure to the reaction for 18 h. However, the mean CeO_2 crystallite size was increased from 7.79 to 8.73 nm, as recorded in Table 2. Furthermore, the diffraction of the alloy peak also shifted to a higher angle of 39.5°, which represented a structural change in the alloy phase. Similarly, Liu et al. (2011) also found a shift from a pure gold diffraction at 38.2° to the Au–Cu alloy at 39.2° after applying the H_2 pretreatment at high temperatures ($T \geq 300$ °C) [36]. With this knowledge, we postulated that more Au–Cu alloy phases were possibly formed in the presence of rich H_2 product gas under the suitable reaction temperature of 300 °C, like the H_2 pretreatment. This alloy formation during the reaction might be one of the factors that preserved the superior stability of the bimetallic Au–Cu catalyst in the stability test. Even though the mechanism of the structural change in the alloy during the steam reforming reaction has not been considered yet, we tried to clarify what changed after exposure to the reaction for a long time by using the available characterizations (XRD and TPO) on the spent catalyst. Interestingly, additional carbon diffractions, including C and Cu_xC, were also detectable, evidenced by the coke formation during the experiment. The diffraction of the metallic Cu also appeared to indicate the reduction of CuO in the alloy phase into reduced form. This was in accordance with the lack of an alloy phase as well, as evidenced by the shifting of the alloy peak towards a higher diffraction angle. However, all of these changes did not seem to strongly affect the stability of the bimetallic catalyst since its activity was still high.

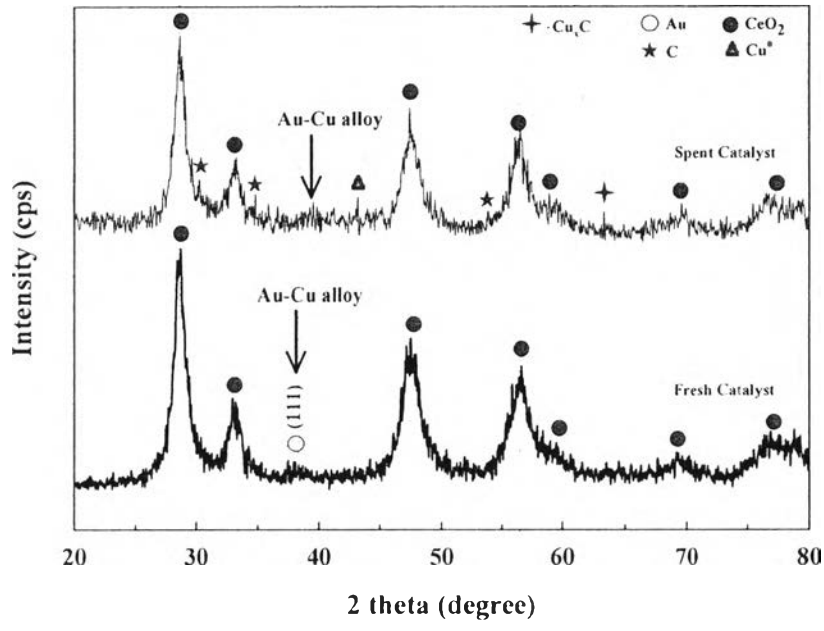

Figure 7.9 XRD patterns of spent 7 wt% Au1Cu3/$Ce_{0.75}Zr_{0.25}O_2$ catalyst after exposure to reaction compared with the fresh catalyst. (Reaction conditions: H_2O/CH_3OH, 2/1; reaction temperature, 300 °C; and time-on-stream per sample, 18 h)

The TPO technique was applied for all spent catalysts after exposure to the reaction in order to check the coke deposited on the catalyst surface, as illustrated in Fig. 7.10. The results presented (i) low-temperature oxidation of 245–278 °C assigned to the oxidation of the poorly polymerized coke deposited on the metal particles and (ii) high-temperature oxidation of 480–493 °C attributed to the highly polymerized coke deposited near the metal–support interphase [2,3,5,37]. Indeed, the Cu catalyst showed two distinct peaks at low temperatures (278 and 342 °C), which were probably due to the coke depositing on different metal sites (i.e. highly dispersed CuO and bulk CuO). Additionally, the percentage of carbon depositon in the spent catalysts was ordered as follows: Cu/CeO_2–ZrO_2 (3.50 %) > Au–Cu/CeO_2–ZrO_2 (1.19 %) > Au/CeO_2–Fe_2O_3 (0.08 %). When focusing on the area under and the intensities of the peaks of coke oxidation for both types, it is clearly seen that the area and intensity of the poorly polymerized coke were much higher, when compared to those of the highly polymerized coke for all spent catalysts. This

can be correlated with the amount of coke oxidation in the spent catalysts, where the amount of poorly polymerized coke (coke depositing on metal sites) was much higher than that of highly polymerized coke (coke depositing on the metal–support interphase) on the catalyst surface. Hence, this is another indication that the coke deposition in the spent catalyst mainly came from the metal sites [37]. Consequently, the $Cu/CeO_2–ZrO_2$ stability was mainly inhibited by coke formation, whereas the $Au/CeO_2–Fe_2O_3$ was not. Although coke was also detectable in the $Au–Cu/CeO_2–ZrO_2$, the amount was still low, so it was not strongly affected. In comparison to the $Cu/CeO_2–ZrO_2$ catalyst, we hypothesized that the advantage of the Au–Cu alloy was probably to inhibit coke formation since Cu normally produces activated O_2 at Au sites, where the oxygen molecules react with the coke, known as coke gasification, where the coke is finally removed. However, unlike this work, some authors found that coke gasification could took place when using very high oxygen vacancies in the support sites [38], performing the O_2 pretreatment in the fresh catalyst [5], and feeding O_2 into the reaction [39]. To better understand the origin of the activated O_2 molecules by Cu, the high activity and stability of the Au–Cu bimetallic catalyst has been improved as a consequence of the charge transfer in metal–metal species, where the presence of highly dispersed CuO species in the bimetallic system formed electronic and chemical interactions with gold; these interactions caused a change in the redox and electronic properties of the Au species, resulting in facilitation of the availability of reactive oxygen [19].

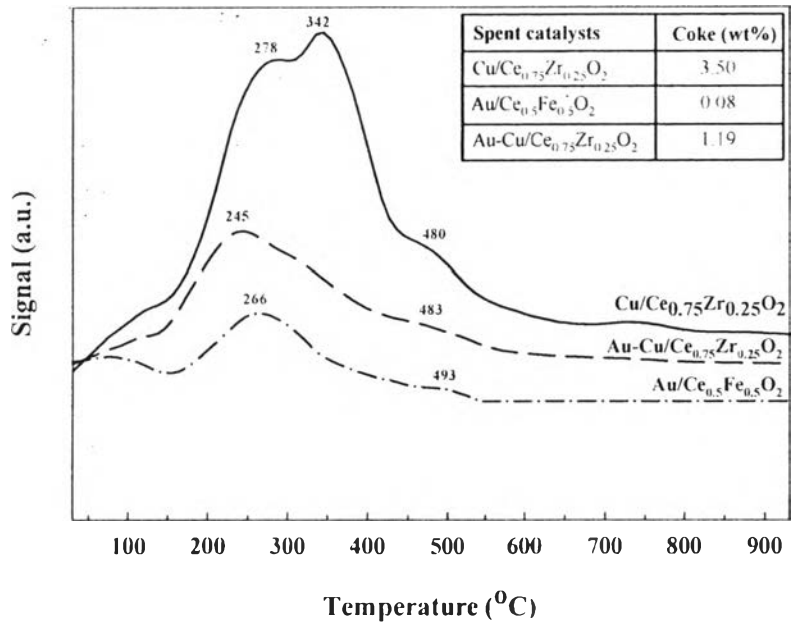

Figure 7.10 TPO profiles of spent catalysts after exposure to reaction compared with the fresh catalyst. (Reaction conditions: H_2O/CH_3OH, 2/1; reaction temperature, 300 °C; and time-on-stream per sample, 18 h)

Previously, it has been reported that Cu or Ag has played an important role in activating oxygen by partially transferring electrons from Cu or Ag to Au, which was the key to promoting the reactions [24,36,40]. Moreover, Liu (2007) proposed an oxygen-transferring model in a chemical reaction for supported Au catalysts containing Cu species, explaining that after the small gold particles were stabilized, the ionic gold species were then increased by O_2 activation, which came from the ability of the Cu species to supply active oxygen during the catalytic reaction, where the oxygen vacancies created on Cu could be filled by oxygen atoms from the feed and leave the activated oxygen on the surface [41]. Finally, this highly reactive oxygen could promote the reaction (as well as SRM) and also continue until the end of the reaction, resulting in the facilitation of stable activity. Accordingly, for this model, it is reasonable to assume that the Au–Cu/CeO_2–ZrO_2 catalyst, in terms of long-term stability via coke gasification, can be similarly correlated to the oxygen activation phenomena.

7.5 Conclusions

A series of Au–Cu/CeO_2–ZrO_2 catalysts were prepared by the deposition-precipitation method, where many parameters, such as Au/Cu atomic ratio, gas pretreatment, total loading, and calcination temperature, were investigated. For the initial studies of 3 wt% (Au 1.5 wt% and Cu 1.5 wt%) loading, the suitable conditions for the homogeneous Au–Cu alloy formation were observed in the Au/Cu ratio of 1/3 without gas pretreatment. Increasing the total metal loading to 7 wt% and decreasing the calcination temperature to 300 °C seemed to slightly enhance the SRM activity. However, the characterization results showed growth of the alloy size at high metal loadings and high calcination temperatures. Furthermore, the reactive sites at the alloy–support interface became less pronounced at a high calcination temperature due to the Cu enrichment on the catalyst surface. The stability observation at T = 300 °C revealed that there was no loss in superior activity of the Au–Cu/CeO_2–ZrO_2 catalyst (100 % methanol conversion), while the presence of metallic Cu and coke formation did not affect the catalytic activity.

7.6 Acknowledgements

The authors acknowledge the contributions and financial support of the following organizations: the Thailand Research Fund through the Royal Golden Jubilee Ph.D. Program (Grant No. PHD/0282/2552); the Center of Excellence on Petrochemical and Advanced Materials, Chulalongkorn University; and The National Research University Project of CHE and the Ratchadaphiseksomphot Endowment Fund (EN276B).

7.7 References

[1] S. Sá, H. Silva, L. Brandão, J.M. Sousa, A. Mendes, Appl. Catal., B 99 (2010) 43–57.

[2] C. Pojanavaraphan, A. Luengnaruemitchai, E. Gulari, Int. J. Hydrogen Energy (2012) 14072–14084.

[3] C. Pojanavaraphan, A. Luengnaruemitchai, E. Gulari, Chem. Eng. J. 192 (2012) 105–113.

[4] S. Pongstabodee, S. Monyanon, A. Luengnaruemitchai, J. Ind. Eng. Chem. 18 (2012) 1272–1279.

[5] C. Pojanavaraphan, A. Luengnaruemitchai, E. Gulari, J. Ind. Eng. Chem. 20 (2014) 961–971.

[6] T. Takahashi, M. Inoue, T. Kai, Appl. Catal., A 218 (2001) 189–195.

[7] A. Basile, A. Parmaliana, S. Tosti, A. Iulianelli, F. Gallucci, C. Espro, J. Spooren, Catal. Today 137 (2008) 17–22.

[8] L. Li, L. Song, H. Wang, C. Chen, Y. She, Y. Zhan, X. Lin, Q. Zheng, Int. J. Hydrogen Energy 36 (2011) 8839–8849.

[9] S. Zeng, Y. Wang, K. Liu, F. Liu, H. Su, Int. J. Hydrogen Energy 37 (2012) 11640–11649.

[10] N. Srisiriwat, S. Therdthianwong, A. Therdthianwong, Int. J. Hydrogen Energy 34 (2009) 2224–2234.

[11] T. Tabakova, G. Avgouropoulos, J. Papavasiliou, M. Manzoli, F. Boccuzzi, K. Tenchev, F. Vindigni, T. Ioannides, Appl. Catal., B 101 (2011) 256–265.

[12] A. Martinez-Arias, M. Fernandez-Garcia, C. Belver, J.C. Conesa, J. Soria, Catal. Lett. 65 (2000) 197–203.

[13] E. Mamontov, T. Egami, R. Brezny, M. Koranne, S. Tyagi, J. Phys. Chem. B 104 (2000) 11110–11116.

[14] F. Zhang, C.H. Chen, J. Am. Ceram. Soc. 89 (2006) 1028–1036.

[15] P. Biswas, D. Kunzru, Chem. Eng. J. 136 (2008) 41–49.

[16] G.C. Bond, C. Louis, D.T. Thompson, Catalysis by Gold, volume 6, Imperial College Press, London, 2006.

[17] J. Llorca, M. Domínguez, C. Ledesma, R.J. Chimentão, F. Medina, J. Sueiras, I. Angurell, M. Seco, O. Rossell, J. Catal. 258 (2008) 187–198.

[18] S.J. Lee, A. Gavriilidis, J. Catal. 206 (2002) 305–313.

[19] T.C. Ou, F.W. Chang, L.S. Roselin, J. Mol. Catal. A: Chem. 293 (2008) 8–16.

[20] S.D. Lin, A.C. Gluhoi, B.E. Nieuwenhuys, Catal. Today 90 (2004) 3–14.

[21] F.W. Chang, T.C. Ou, L.S. Roselin, W.S. Chen, S.C. Lai, H.M. Wu, J. Mol. Catal. A: Chem. 313 (2009) 55–64.

[22] R.P. Hernández, A.G. Martínez, C.E.G. Wing, Int. J. Hydrogen Energy 32 (2007) 2888–2894.

[23] C. Pojanavaraphan, A. Luengnaruemitchai, E. Gulari, Int. J. Hydrogen Energy 38 (2013) 1348–1362.

[24] X. Liu, A. Wang, T. Zhang, D.S. Su, C.Y. Mou, Catal. Today 160 (2011) 103–108.

[25] B.M. Reddy, A. Khan, Catal. Surv. from Asia 9 (2005) 155–171.

[26] M. Yashima, H. Arashi, M. Kakihana, M. Yoshimura, J. Am. Ceram. Soc. 75 (1992) 1541–1549.

[27] K.R. Souza, A.F.F. Lima, F.F. Sousa, L.G. Appel, Appl. Catal., A 340 (2008) 133–139.

[28] G.R. Rao, H.R. Sahu, J. Chem. Sci. 113 (2001) 651–658.

[29] R. Zanella, S. Giorgio, C.H. Shin, C.R. Henry, C. Louis, J. Catal. 222 (2004) 357–367.

[30] F.W. Chang, L.S. Roselin, T.C. Ou, Appl. Catal., A 334 (2008) 147–155.

[31] A.C. Gluhoi, X. Tang, P. Marginean, B.E. Nieuwenhuys, Top. Catal. 39 (2006) 101–110.

[32] J. Kugai, J.T. Miller, N. Guo, C. Song, Appl. Catal., B 105 (2011) 306–316.

[33] R.J. Chimentão, F. Medina, J.L.G. Fierro, J. Llorca, J.E. Sueiras, Y. Cesteros, P. Salagre, J. Mol. Catal. A: Chem. 274 (2007) 159–168.

[34] F. Wang, G. Lu, Int. J. Hydrogen Energy 35 (2010) 7253–7260.

[35] M. Mavrikakis, P. Stoltze, J.K. Nørskov, Catal. Lett. 64 (2000) 101.

[36] X. Liu, A. Wang, L. Li, T. Zhang, C.Y. Mou, J.F. Lee, J. Catal. 278 (2011) 288–296.

[37] A. Luengnaruemitchai, A. Kaengsilalai, Chem. Eng. J. 144 (2008) 96–102.

[38] S. Patel, K.K. Pant, J. Power Sources 159 (2006) 139–143.

[39] T. Valdes-Solis, G. Marban, A.B. Fuertes, Catal. Today 116 (2006) 354–360.

[40] W. Li, A. Wang, X. Liu, T. Zhang, Appl. Catal., A 433–434 (2012) 146–151.

[41] W. Liu, Chem. Eng. Sci. 62 (2007) 3502–3512.